Positioning in 6G Networks: Can a Standalone RIS Reduce the Need for Dense Base Station Deployments?

Simon Johnsson[1,*], Yves Teganya[2], Payal Gupta[1], Sara Sandberg[2] and Jaap van de Beek[1]

[1]Luleå University of Technology, Luleå, Sweden
[2]Ericsson Research, Luleå, Sweden

Abstract

This paper investigates the role of standalone Reconfigurable Intelligent Surfaces (RIS) in enhancing positioning capabilities in 6G networks. A standalone RIS differs from a conventional RIS in that the former is not controlled by the network or any other external node. Rather, it operates *autonomously* and its configurations and location are known to the network. We explore RIS as a tool to enable positioning through Time Difference of Arrival (TDoA) estimation with fewer base stations (BSs), leveraging its ability to act as a virtual BS. A theoretical framework is developed using the Cramér-Rao Lower Bound (CRLB) to analyze the estimation accuracy under various deployment scenarios and parameter settings. Our findings demonstrate that while RIS does not inherently improve TDoA accuracy, it facilitates sparser BS deployments by requiring only one BS and one RIS for effective estimation of TDoA. Additionally, we evaluate the impact of system parameters such as the number of subcarriers, pilot spacing, and RIS elements, identifying subcarrier spacing as the most influential factor for improving the TDoA estimate. These insights highlight the potential of RIS to complement conventional BS deployments and advance 6G TDoA estimation systems.

Keywords

6G Networks, Positioning, Reconfigurable Intelligent Surfaces (RIS), Cramer-Rao Lower Bound (CRLB)

1. Introduction

The inference of user location in cellular networks has been a prominent research focus since the early generations of cellular technology in the 1990s. As the 6th generation (6G) of cellular networks approaches, there are renewed plans to expand localization functionalities. Current systems already offer various localization capabilities through a wide range of solutions. Common positioning techniques include measurements of Time-of-Arrival (ToA), Time-Difference-of-Arrival (TDoA), Angle-of-Arrival (AoA), Received Signal Strength (RSS), and combinations of multiple kinds of measurements [1, 2, 3].

The various measurements mentioned above have their strengths and weaknesses, and in this paper we are considering TDoA because it is a type which is used in current 5G systems. It is often used because it reduces the need for synchronization between BSs and the UE, because relative difference in time-of-flight are considered, not the absolute times [4].

One challenge in TDoA estimation is that the UE must be in line-of-sight (LoS) to two BSs and TDoA-based methods typically necessitate a dense deployment of BSs [1] to do positioning. For exmaple, 3D localization based on TDoA estimates requires at least 3 TDoA measurements, which involves at least 4 BSs. This paper explores the potential of incorporating Reconfigurable Intelligent Surfaces (RIS) into the network to reduce the need for such dense BS deployments. A RIS consists of a grid of reflective elements capable of dynamically altering their reflective properties. By adjusting the phase of the incident signal, a RIS can control how signals interact with the propagation environment, optimizing how the signal is reflected[5].

A RIS offers a significant potential for both communication and positioning. In communication, it enhances the signal-to-noise ratio (SNR) by directing signals toward targets or around obstacles. For positioning, a RIS can similarly improve SNR and facilitate the identification of signals reflected from

WIPHAL'25: Work-in-Progress in Hardware and Software for Location Computation June 10–12, 2025, Rome, Italy
*Corresponding author.
simon.johnsson@ltu.se (S. Johnsson); yves.teganya@ericsson.com (Y. Teganya); payal.gupta@ltu.se (P. Gupta); sara.sandberg@ericsson.com (S. Sandberg); jaap.vandebeek@ltu.se (J. van de Beek)
© 2025 Copyright for this paper by its authors. Use permitted under Creative Commons License Attribution 4.0 International (CC BY 4.0).

CEUR Workshop Proceedings ceur-ws.org ISSN 1613-0073

CEUR-WS.org/Vol-3980/paper3.pdf

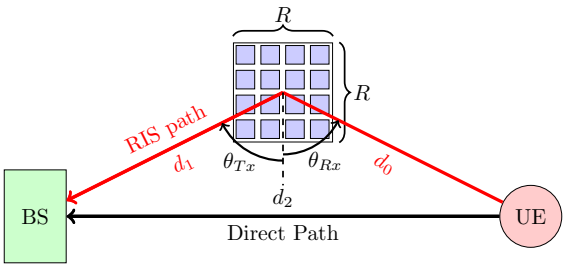

Figure 1: Our system model. The black arrow indicates the direct signal path between the transmitter and receiver, while the red arrows represent signal paths reflected via the RIS. The RIS consists of a grid of $R \times R$ reflective elements.

the RIS. This capability enables a RIS to function as a virtual BS, expanding opportunities for precise positioning even in complex environments.

The field of RIS research has been around for a few years and has gained significant attention in academia, resulting in a growing body of research. A common assumption in many positioning studies is that the RIS is connected to the network and can be controlled in real time [6]. This connectivity enhances the functionality of the RIS by allowing it to adapt dynamically to its surroundings. However, it also introduces additional complexity due to the need for network integration. This added complexity, including complicated channel estimation, has made the industry more skeptical towards RIS because it does not add much more functionality than the current relays and may not contribute to much cost-savings if it is needed to be fully integrated into the network.

In this work, we focus on an alternative and novel approach which to our knowledge has not been studied yet. We consider a standalone RIS that operates independently of the network. Instead of real-time control, the RIS employs a predefined set of reflection patterns known to the network. This reduces the complexity of the system and deployment, while still enabling useful positioning functionality. The reduction in network complexity comes because there is no form of communication between the RIS and the network after the over-the-air initialization of the RIS.

Clearly, replacing an (active) base station with a (passive) RIS will degrade the positioning accuracy, but in this paper we show that the performance loss can be kept surprisingly small. Hence RIS-aided deployments can often be justified for the above-mentioned reasons of complexity.

We look to assess the performance of TDoA estimation with RIS using the Cramér-Rao Lower Bound (CRLB), a method commonly applied in classical BS positioning scenarios [7]. Although there are studies that explore the CRLB in the context of RIS [8], these studies typically focus on deriving bounds for the positioning accuracy directly. In contrast, our approach examines intermediate parameters, in this case time-difference-of-arrival (TDoA) information, providing additional insights into the underlying mechanisms. This is done in order to get an insight into how the TDoA estimation effect the positioning capabilities and this TDoA estimate can be used either by itself or with additional estimates to perform positioning, as commonly used in 5G networks today.

2. System model

2.1. RIS-BS system model

We consider an Orthogonal Frequency Division Multiplexing (OFDM) system where both the transmitter and receiver are equipped with single omnidirectional antennas. The RIS consists of $R \times R$ reflective elements (or unit cells), and each element is able to induce a controllable phase shift to the incident signal independently. In this paper, to keep down the mathematical complexity, an Additive White Gaussian Noise (AWGN) channel with two paths is assumed: a direct path from the user equipment (UE) to the base station (BS) represented by the black line, and a path reflected through the RIS represented

by the red line. These modeled paths are illustrated in Figure 1.[1]

Assuming that the pilots used in the estimation are known and with modulus one, they can be removed at the receiver and because the system considered is an OFDM system where there are multiple subcarriers, $N > 1$, and symbols $M \geq 1$, we can start by considering just one carrier, the n-th subcarrier and the m-th symbol. The received signal, $y_{n,m}$, can then be expressed as

$$y_{n,m} = \sqrt{P} e^{-j\varepsilon} \left[\rho_0 \varphi_n(\tau_0) + \rho_1 \gamma_{n,m}(\theta_{\text{Rx}}) \varphi_n(\tau_1) \right] + w_{n,m}, \tag{1}$$

where P is the transmit power per subcarrier, ρ_0 and ρ_1 represent the attenuation along the direct and RIS paths, respectively. $\varphi_n(\tau) = e^{-j2\pi f_n \tau}$ represents the phase shift of the n-th subcarrier at time τ, and the subcarrier frequency is $f_n = f_0 + n\Delta f$, with f_0 as the carrier frequency and Δf as the subcarrier spacing. The parameter τ_0 denotes the time-of-flight between the UE and the BS, τ_1 is the time-of-flight via the RIS, and $\varepsilon \sim U(-\pi, \pi)$ is a random variable representing various phase offsets as for example synchronization errors. We assume that the BS and RIS have known positions and orientations and also that the power, P, and the reflective angle, θ_{Tx}, are known.

The model is general enough to accommodate various RIS beamforming patterns. This is achieved by combining steering vectors (representing the incident and reflected signals at the RIS) with the phase shifts of the RIS elements, as described in [9]. The resulting RIS channel is modeled as

$$\gamma_{n,m}(\theta_{\text{Rx}}) = \sum_{r=1}^{R} e^{j2\pi \frac{\delta}{\lambda_n} (\sin\theta_{\text{Tx}} + \sin\theta_{\text{Rx}})(r-1) + j\psi_r^{(m)}}, \tag{2}$$

where $\gamma_{n,m}(\theta_{\text{Rx}})$ is the diagonal element of the matrix, $\mathbf{\Gamma}(\theta_{\text{Rx}}) \in \mathbb{C}^{NM \times NM}$, θ_{Tx} and θ_{Rx} are the angles between the signal direction and the RIS surface (reflected and impinging, respectively). The parameter δ is for the width and height of each RIS cell assuming it is square shaped, λ_n is the wavelength for subcarrier n, and $\psi_r^{(m)}$ is the reflection coefficient of the r-th RIS cell widthwise for symbol m. In this study, M random radiation patterns are used, with one pattern per symbol, m.

In this paper, we are only interested in the time based parameters for estimation, therefore the unknown parameters of interest are $\boldsymbol{\zeta} = [\tau_0, \tau_1]$ and the unknown nuisance parameters are $\boldsymbol{\eta} = [\theta_{\text{Rx}}, \rho_0, \rho_1, \varepsilon]$. The angle θ_{Rx} also carries information regarding the UE position, but it is not evaluated in this paper to keep the paper concise.

Due to the orthogonality of the OFDM system, each subcarrier and symbol are independent, resulting in a column-vector representing the channel, $\boldsymbol{h}(\boldsymbol{\zeta}, \boldsymbol{\eta})$. The entire system can then be represented in vector form using blocks of vectors, where each block corresponds to all N subcarriers for a single symbol m ($0 \leq m \leq M$). Because of this, (1) can be rewritten in matrix/vector form as

$$\boldsymbol{y} = \boldsymbol{h}(\boldsymbol{\zeta}, \boldsymbol{\eta}) + \boldsymbol{w}, \tag{3}$$

where the channel vector is given by

$$\boldsymbol{h}(\boldsymbol{\zeta}, \boldsymbol{\eta}) = \sqrt{P} e^{-j\varepsilon} \left[\rho_0 \boldsymbol{\varphi}(\tau_0) + \rho_1 \mathbf{\Gamma}(\theta_{\text{Rx}}) \boldsymbol{\varphi}(\tau_1) \right], \tag{4}$$

and $\boldsymbol{y} \in \mathbb{C}^{NM \times 1}$ is the vector of received signals, $\boldsymbol{h}(\boldsymbol{\zeta}, \boldsymbol{\eta}) \in \mathbb{C}^{NM \times 1}$ is the channel vector, and $\boldsymbol{w} \in \mathbb{C}^{NM \times 1}$ represents Gaussian noise with variance σ^2.

2.2. Two-BS system model

To evaluate the performance of RIS-aided TDoA estimations, we compare it with a more conventional reference positioning system, specifically a two-BS scenario [10]. To ensure a fair comparison, the RIS in the previous model is replaced with a BS and this system is also modeled for the uplink case. In this

[1] Although the model is described for the uplink case, it is equally applicable to the downlink scenario by inverting the roles of the transmitter and receiver.

setup, a signal is transmitted from a UE and received by two separate BSs. The received signal can be expressed as

$$\boldsymbol{y}^{\text{BS}} = \begin{bmatrix} \boldsymbol{y}_1^{\text{BS}} \\ \boldsymbol{y}_2^{\text{BS}} \end{bmatrix} = \sqrt{P} \begin{bmatrix} e^{-j\varepsilon_1}\rho_1^{\text{BS}}\boldsymbol{\varphi}(\tau_1^{\text{BS}}) \\ e^{-j\varepsilon_2}\rho_2^{\text{BS}}\boldsymbol{\varphi}(\tau_2^{\text{BS}}) \end{bmatrix} + \boldsymbol{w}^{BS}, \tag{5}$$

or equivalently, in matrix/vector form

$$\boldsymbol{y}^{\text{BS}} = \boldsymbol{h}^{\text{BS}}(\boldsymbol{\zeta}^{\text{BS}}, \boldsymbol{\eta}^{\text{BS}}) + \boldsymbol{w}^{BS}, \tag{6}$$

where ρ_i^{BS} and τ_i^{BS} represents the attenuation and the ToA at the i-th BS, respectively. For this system, there are two independent phase offsets, ε_1 and ε_2, corresponding to the two BSs.

The vector of parameters of interest are defined as $\boldsymbol{\zeta}^{\text{BS}} = [\tau_1^{\text{BS}}, \tau_2^{\text{BS}}]$ and the nuisance parameter vector is defined as $\boldsymbol{\eta}^{\text{BS}} = [\rho_1^{\text{BS}}, \rho_2^{\text{BS}}, \epsilon_1^{\text{BS}}, \epsilon_2^{\text{BS}}]$.

3. Cramer-Rao Lower Bound

In order to calculate the Cramer-Rao lower bound (CRLB), we need to first describe the log-likelihood function of the system [11]. As recall, the system model in (3) is an AWGN-channel which means that measurements in $\boldsymbol{y}$ has the following Gaussian distribution

$$\boldsymbol{y} \sim N\big(\boldsymbol{h}(\boldsymbol{\zeta}, \boldsymbol{\eta}), \sigma^2 \boldsymbol{I}\big), \tag{7}$$

where $\boldsymbol{h}(\boldsymbol{\zeta}, \boldsymbol{\eta})$ is described in the previous section as equation (4). The log-likelihood function, $\Lambda(\boldsymbol{\zeta}, \boldsymbol{\eta})$, is

$$\Lambda(\boldsymbol{\zeta}, \boldsymbol{\eta}) = A - \frac{1}{\sigma^2}||\boldsymbol{y} - \boldsymbol{h}(\boldsymbol{\zeta}, \boldsymbol{\eta})||^2, \tag{8}$$

where A is a constant which will disappear in the construction of the Fisher Information matrix (FIM).

To describe the amount of information the observed signal carries about each unknown parameter, both desired and nuisance, the FIM[11] is created for $\boldsymbol{\vartheta} = [\boldsymbol{\zeta}, \boldsymbol{\eta}]$ as

$$[\mathbb{I}]_{i,j} = -E\left\{ \frac{\partial^2 \Lambda}{\partial \boldsymbol{\vartheta}_i \partial \boldsymbol{\vartheta}_j} \right\}. \tag{9}$$

The elements from the FIM given in (9) are given in appendix A.

The FIM has two different ToA parameters, τ_0 and τ_1, but we are interested in estimating the TDoA, which is $\Delta\tau \triangleq \tau_1 - \tau_0$, and the other parameters should be unchanged. With this knowledge, we get the parameter function, $g(\boldsymbol{\vartheta}) = [\tau_1 - \tau_0, \theta_{\text{Rx}}, \rho_0, \rho_1, \varepsilon]^T$ and the Jacobian matrix becomes

$$\boldsymbol{J} = \frac{\partial g(\boldsymbol{\vartheta})}{\partial \boldsymbol{\vartheta}} = \begin{bmatrix} \begin{bmatrix} -1 & 1 \end{bmatrix} & \mathbf{0}_{1\times 4} \\ \mathbf{0}_{4\times 2} & \mathbf{I}_{4\times 4} \end{bmatrix}. \tag{10}$$

The new FIM, constructed [11, Section 3.8] by

$$\mathbb{I}_{\text{new}} = \boldsymbol{J}\mathbb{I}\boldsymbol{J}^T, \tag{11}$$

becomes a 5×5 matrix which depends on the TDoA instead of the two ToA's. Now there is only one parameter of interest and $\boldsymbol{\zeta} = [\Delta\tau]$, the CRLB is given by the inverse of the FIM, $\mathbb{I}_{\text{new}}^{-1}$, and because only the TDoA is of interest, the inverse of the top left element needs to be calculated using e.g. the Schur compliment [12].

For the two-BS case, the log-likelihood function becomes

$$\Lambda(\boldsymbol{\zeta}^{\text{BS}}, \boldsymbol{\eta}^{\text{BS}}) = A_{\text{BS}} - \frac{1}{\sigma^2}||\hat{\boldsymbol{y}}^{\text{BS}} - \boldsymbol{h}^{\text{BS}}(\boldsymbol{\zeta}^{\text{BS}}, \boldsymbol{\eta}^{\text{BS}})||^2, \tag{12}$$

which can be seen to have the same form as the RIS-BS case. In similar fashion to the previous case equations (9)-(11) can be used to calculate the corresponding CRLB.

Table 1
Parameter values of each parameter sweep

Sweep param	N	M	$N_{\Delta f}$	R
N	1-256	4	10	16
M	64	2-10	10	16
$N_{\Delta f}$	64	4	1-20	16
R	64	4	10	8-24

4. Results

4.1. Computational prerequisites

To calculate the bounds, we choose the carrier frequency $f_0 = 3.5$ GHz and the subcarrier spacing $\Delta f = 30$ kHz. Also power per subcarrier is chosen as $P = \frac{10}{N}$mW and the noise power is at the thermal noise floor $\sigma^2 = 4k_BT\Delta f$ where T is room temperature and k_B is the Boltzmann constant.

The models in (3) and (6) are valid under the far-field assumption, which means that the UE or BS cannot be closer than the Fraunhofer distance, $2(R\delta)^2/\lambda$, to the RIS for the far-field assumption to hold.

As can be seen in the previous section, our models do not assume any particular propagation model, but to compute the bounds, some kind of propagation model needs to be selected. In this section, the free-space path loss model is adopted as

$$\rho = \frac{A_{\text{Rx}}A_{\text{Tx}}}{d^\alpha \lambda^2}, \tag{13}$$

where A_{Tx} and A_{Rx} are the effective area of the transmitter and receiver, respectively, d is the distance between transmitter and receiver, $\alpha = 2$ is the free-space path loss exponent, and λ is the wavelength of the transmitted signal. For the case with two BS, we have two omnidirectional antennas with effective area A for both transmitter and receiver, i.e., $A_{\text{Tx}} = A_{\text{Rx}} = \frac{\lambda^2}{4\pi}$ and the path gain equation becomes

$$\rho_i^{\text{BS}} = \frac{\lambda^2}{16\pi^2 d_i^2}, \tag{14}$$

where d_i is the distance between the ith BS and the UE. For the RIS-BS case, the direct path becomes the same as in the previous case, but the path through the RIS gets a different effective area for one of the transmitter and receiver, this is because one of the sides will be an omnidirectional antenna while the other one will take form from the RIS and becomes $A_{ix}^{\text{RIS}} = R^2\delta^2 cos\theta_{ix}$. Moreover, the path loss will be cascaded for both the paths to and from the RIS. The resulting path gain equation becomes

$$\rho_1 = \frac{A_{\text{Tx}}A_{\text{Rx}}^{\text{RIS}}}{d_{d_0}^2\lambda^2}\frac{A_{\text{Rx}}A_{\text{Tx}}^{\text{RIS}}}{d_{d_1}^2\lambda^2} = \frac{(R^2\delta^2)^2\cos\theta_{\text{Tx}}\cos\theta_{\text{Rx}}}{16\pi^2 d_{d_0}^2 d_{d_1}^2}. \tag{15}$$

Here for these calculations the size of the RIS-elements are set to $\delta = \lambda/2$.

4.2. Comparison of two RIS-BS-geometries

First, we evaluate the geometry of the setup, focusing on the placement of the BSs and RIS relative to the UE. Specifically, we examine how different RIS and BS placements, distance between them and orientation, affect the CRLB of the TDoA estimate compared to a system with two BSs. For this geometric analysis, we consider a 40 m $\times$ 30 m area. Two configurations are studied: one where the BS and RIS are far apart and another where they are positioned close to each other.

The TDoA error bound, square root of the CRLB, of the two scenarios are shown where Figure 2a corresponds to a spread out scenario, while Figure 2b represents the close in case. The white region around the RIS represents the near-field zone of the RIS where the model used in this paper is not valid.

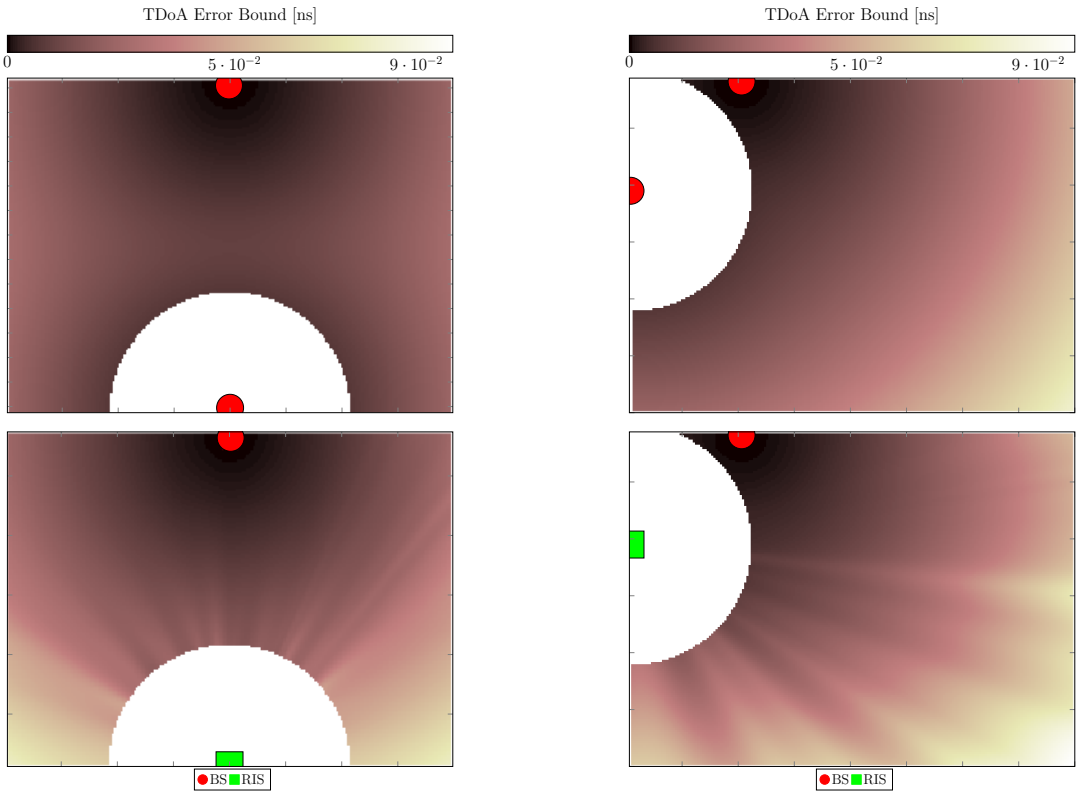

(a) Sparse BS and RIS deployment.

(b) Dense BS and RIS deployment.

Figure 2: Maps depicting the TDoA error bound, square root of the CRLB of different scenarios. All four maps are of the size 30×40 m.

This region was also excluded from the two-BS case—not due to near-field effects, but for computational efficiency and to maintain consistency between the two scenarios.

As expected, the CRLB is higher (worse) when the angle between signal from the UE and the normal of the RIS is close to 90 degrees, as the UE perceives a smaller effective area of the RIS. Additionally, the CRLB near the BS in the RIS-BS scenario is comparable to the CRLB near the same BS in the two-BS case. This indicates that the RIS itself does not directly improve the CRLB. Instead, the RIS facilitates the TDoA estimation, allowing the system to operate with just one BS.

The effects of the RIS radiation pattern are also evident in the maps, where radial lines radiating from the RIS reflect the superposition of the patterns used in the CRLB calculation. This superposition emphasizes the importance of utilizing the full angular space of the RIS to achieve a more homogeneous bound of the CRLB.

4.3. Sensitivity of the CRLB to changes of system parameters

Secondly, the impact of different parameters on the CRLB is evaluated. The parameters that are considered are the number of subcarriers N, the number of symbols M, pilot spacing in number of subcarriers $N_{\Delta f}$, and the number of RIS elements $R \times R$. To get some indications on how the different parameters effect the bound, a parameter sweep is performed for each of the parameters of interest. For each of the sweeps, the BS is located at (20 m, 0 m) and the RIS is placed at (20 m, 30 m), the parameters used in each sweep can be found in Table 1. Two possible UE locations are considered at (5 m, 5 m) for scenario A and (5 m, 25 m) for scenario B, see Figure 3.

The resulting TDoA error bound of the parameter sweep are presented in Figures 4a and 4b for the UE located at (5 m, 5 m) and (5 m, 25 m), respectively. These results reveal that the CRLB improves as the evaluated parameters increase. Additionally, the performance gap between the RIS-BS and two-BS case narrows with increasing parameter values.

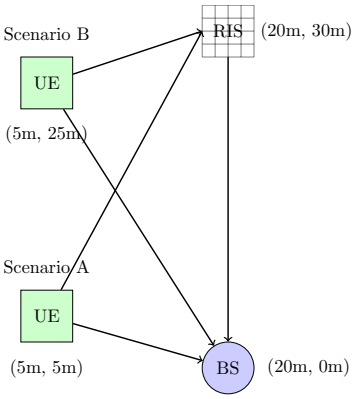

Figure 3: Simulation setup used for the parameter sweep evaluations, with the BS, RIS, and UE locations for Scenarios A and B.

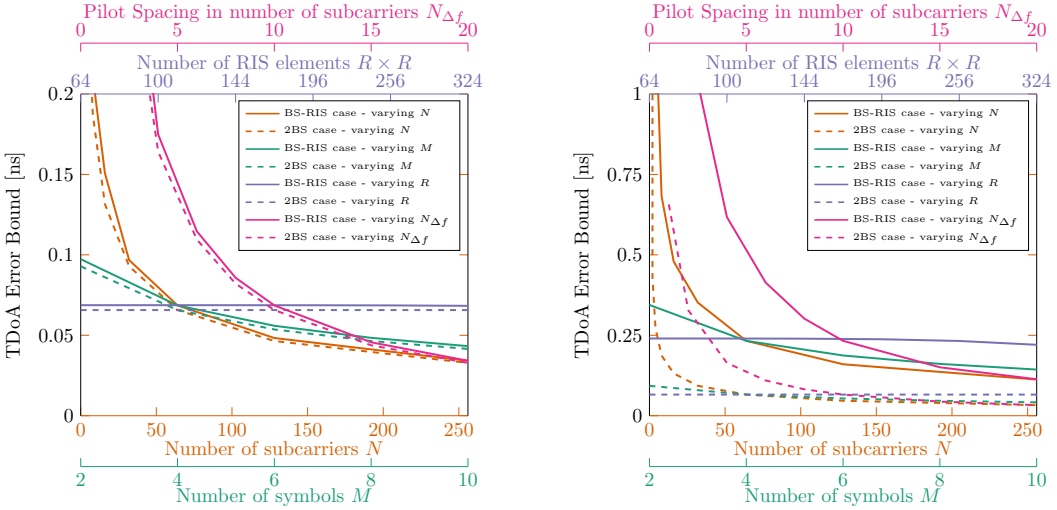

(a) Scenario A

(b) Scenario B

Figure 4: CRLB as a function of different varying parameters for the UE located at (5 m, 5 m) and (5 m, 25 m) in (a) and (b), respectively. The orange curves are for number of subcarriers, N, the green for the number of symbols, M, the purple for the total number of RIS elements, $R \times R$, and the pink for the pilot spacing, $N_{\Delta f}$.

The sweeps indicate that parameters related to frequency, the number of subcarriers, and pilot spacing have the most significant impact on the CRLB. The improvement with an increased number of subcarriers is straightforward, as it directly corresponds to an increase in the system bandwidth. For subcarrier spacing, the improvement arises from increased spectral efficiency due to the expanded range between the lowest and highest frequencies. Notably, increasing subcarrier spacing does not add overhead to the system, as the same number of subcarriers is used for positioning purposes.

Counterintuitively, it can be seen that a large number of RIS elements does not significantly improve the CRLB. This could be due to that the reflected path which goes through the RIS is much weaker than the direct path. This means to that a change in RIS size has minor impact on the total power collected by the receiver. The same conclusion can be drawn if we look at figure 2a, where only the distance to the BS affects the bound and not the distance to the RIS.

When comparing results (in Figures 4a and 4b) at the two UE locations, Scenarios A and B seen in Figure 3, we observe that when the UE is located at (5 m, 5 m), Scenario A—where the UE is close to the BS—the performance of the RIS-BS case is more similar to the two-BS case. However, when the UE is located at (5 m, 25 m), Scenario B, where the UE is far from the BS, the CRLB is higher, reflecting the greater challenge of achieving accurate positioning in this case.

5. Conclusion

As demonstrated in this paper, a standalone RIS is not primarily intended to improve the TDoA estimation accuracy. Instead, its value lies in enabling a sparser deployment of base stations, while making it possible to estimate the TDoA to a reasonable accuracy. As each RIS may act as a virtual BS, 3D positioning based on TDoA measurements can be performed with LoS to 3 BSs combined with a RIS (or even 2 BSs combined with 2 RISs) as an alternative to having LoS to 4 BSs.

Additionally, while not covered in detail in this study, it is worth noting that RISs can also provide angular information, which is be useful for positioning. This angular information can be exploited even when the base station is a simpler setup with fewer antennas.

Regarding the parameter sweeping performed in this study, it was observed that when the UE is near the BS, the performance in TDoA estimation with one BS and one RIS is only slightly worse than that with two BSs. The results also show that increasing any of the parameters–number of subcarriers, number of symbols, number of RIS-elements and pilot spacing–improves the CRLB bound, with number of subcarriers and pilot spacing having the most significant impact. If only one of these two parameters is to be increased, subcarrier spacing should be prioritized, as it does not increase the number of pilots required for positioning, leaving more resources available for communication.

Acknowledgments

This research is financially supported by the European Regional Development Fund and the Green Transition North – circular economy (GTN—CE)-project (no. 20359796).

Declaration on Generative AI

During the preparation of this work, the authors used ChatGPT in order to correct grammar and spelling. After using these tool, the authors reviewed and edited the content as needed and take full responsibility for the publication's content.

References

[1] F. Gustafsson, F. Gunnarsson, Positioning using time-difference of arrival measurements, in: 2003 IEEE International Conference on Acoustics, Speech, and Signal Processing, 2003. Proceedings. (ICASSP '03)., volume 1, IEEE, Hong Kong, China, 2003, pp. VI–553–6. URL: http://ieeexplore.ieee.org/document/1201741/. doi:10.1109/ICASSP.2003.1201741.

[2] R. Peng, M. L. Sichitiu, Angle of Arrival Localization for Wireless Sensor Networks, in: 2006 3rd Annual IEEE Communications Society on Sensor and Ad Hoc Communications and Networks, IEEE, Reston, VA, 2006, pp. 374–382. URL: https://ieeexplore.ieee.org/document/4068140/. doi:10.1109/SAHCN.2006.288442.

[3] P. Tarrio, A. M. Bernardos, J. A. Besada, J. R. Casar, A new positioning technique for RSS-Based localization based on a weighted least squares estimator, in: 2008 IEEE International Symposium on Wireless Communication Systems, IEEE, Reykjavik, Iceland, 2008, pp. 633–637. URL: http://ieeexplore.ieee.org/document/4726133/. doi:10.1109/ISWCS.2008.4726133.

[4] F. Zafari, A. Gkelias, K. K. Leung, A Survey of Indoor Localization Systems and Technologies, IEEE Communications Surveys & Tutorials 21 (2019) 2568–2599. URL: https://ieeexplore.ieee.org/document/8692423/. doi:10.1109/COMST.2019.2911558.

[5] Q. Wu, S. Zhang, B. Zheng, C. You, R. Zhang, Intelligent Reflecting Surface-Aided Wireless Communications: A Tutorial, IEEE Transactions on Communications 69 (2021) 3313–3351. URL: https://ieeexplore.ieee.org/document/9326394/. doi:10.1109/TCOMM.2021.3051897.

[6] E. Bjornson, H. Wymeersch, B. Matthiesen, P. Popovski, L. Sanguinetti, E. De Carvalho, Reconfigurable Intelligent Surfaces: A signal processing perspective with wireless applications, IEEE

Signal Processing Magazine 39 (2022) 135–158. URL: https://ieeexplore.ieee.org/document/9721205/. doi:10.1109/MSP.2021.3130549.

[7] A. Yeredor, E. Angel, Joint TDOA and FDOA Estimation: A Conditional Bound and Its Use for Optimally Weighted Localization, IEEE Transactions on Signal Processing 59 (2011) 1612–1623. URL: http://ieeexplore.ieee.org/document/5678660/. doi:10.1109/TSP.2010.2103069.

[8] D. Gürgünoğlu, E. Björnson, G. Fodor, Joint Pilot-Based Localization and Channel Estimation in RIS-Aided Communication Systems, IEEE Wireless Communications Letters 13 (2024) 3119–3123. URL: https://ieeexplore.ieee.org/document/10664026/. doi:10.1109/LWC.2024.3454370.

[9] J. He, H. Wymeersch, T. Sanguanpuak, O. Silven, M. Juntti, Adaptive Beamforming Design for mmWave RIS-Aided Joint Localization and Communication, in: 2020 IEEE Wireless Communications and Networking Conference Workshops (WCNCW), IEEE, Seoul, Korea (South), 2020, pp. 1–6. URL: https://ieeexplore.ieee.org/document/9124848/. doi:10.1109/WCNCW48565.2020.9124848.

[10] R. M. Vaghefi, R. M. Buehrer, On the CRLB of TDOA/FDOA estimation from MIMO signals, in: 2016 IEEE/ION Position, Location and Navigation Symposium (PLANS), IEEE, Savannah, GA, 2016, pp. 772–778. URL: http://ieeexplore.ieee.org/document/7479772/. doi:10.1109/PLANS.2016.7479772.

[11] S. M. Kay, Fundamentals of statistical signal processing, Prentice Hall signal processing series, Prentice-Hall PTR, Englewood Cliffs, N.J, 1993.

[12] R. Fewster, P. Jupp, Information on parameters of interest decreases under transformations, Journal of Multivariate Analysis 120 (2013) 34–39. URL: https://linkinghub.elsevier.com/retrieve/pii/S0047259X13000961. doi:10.1016/j.jmva.2013.05.010.

A. Elements of the FIM for the RIS-BS-case

For compactness and readability, $\boldsymbol{\varphi} \triangleq \boldsymbol{\varphi}(\tau_1)^* \odot \boldsymbol{\varphi}(\tau_0)$ and $\frac{\partial \boldsymbol{\Gamma}^H}{\partial \theta_{\text{Rx}}}$ is kept as it is. The FIM is symmetric, so describing the elements of the upper triangle part of the matrix is sufficient, $\text{tr}\big(\boldsymbol{A}\big)$ is the trace of the matrix A. $\boldsymbol{f}_N$ is a vector made of f_n for all subcarriers, $(1 \leq n \leq N)$.

$$
\begin{aligned}
[\mathbb{I}]_{\tau_0,\tau_0} &= 8\pi^2 P \rho_0^2 \sigma^{-2} \boldsymbol{f}_N^T \boldsymbol{f}_N \\
[\mathbb{I}]_{\tau_0,\tau_1} &= 8\pi^2 P \rho_0 \rho_1 \sigma^{-2} \big(\boldsymbol{f}_N \odot \boldsymbol{f}_N\big)^T \text{Re}\big[\boldsymbol{\Gamma}^H \boldsymbol{\varphi}\big] \\
[\mathbb{I}]_{\tau_0,\rho_0} &= 0 \\
[\mathbb{I}]_{\tau_0,\rho_1} &= 4\pi P \rho_0 \sigma^{-2} \boldsymbol{f}_N^T \text{Im}\big[\boldsymbol{\Gamma}^H \boldsymbol{\varphi}\big] \\
[\mathbb{I}]_{\tau_0,\theta_{\text{Rx}}} &= 4\pi P \rho_0 \rho_1 \sigma^{-2} \boldsymbol{f}_N^T \text{Im}\big[\frac{\partial \boldsymbol{\Gamma}^H}{\partial \theta_{\text{Rx}}} \boldsymbol{\varphi}\big] \\
[\mathbb{I}]_{\tau_0,\varepsilon} &= 4\pi P \rho_0 \sigma^{-2} \boldsymbol{f}_N^T \big[\rho_0 + \rho_1 \text{Re}\big(\boldsymbol{\Gamma}^H \boldsymbol{\varphi}\big)\big] \\
[\mathbb{I}]_{\tau_1,\tau_1} &= 8\pi^2 P \rho_1^2 \sigma^{-2} \big(\boldsymbol{\Gamma}^H \boldsymbol{f}_N\big)^T \big(\boldsymbol{\Gamma} \boldsymbol{f}_N\big) \\
[\mathbb{I}]_{\tau_1,\rho_0} &= 4\pi P \rho_1 \sigma^{-2} \boldsymbol{f}_N^T \text{Im}\big[\boldsymbol{\Gamma} \boldsymbol{\varphi}^*\big] \\
[\mathbb{I}]_{\tau_1,\rho_1} &= 0 \\
[\mathbb{I}]_{\tau_1,\theta_{\text{Rx}}} &= 4\pi P \rho_1^2 \sigma^{-2} || \boldsymbol{f}_N \text{Im}\big[\frac{\partial \boldsymbol{\Gamma}^H}{\partial \theta_{\text{Rx}}} \boldsymbol{\Gamma}\big] || \\
[\mathbb{I}]_{\tau_1,\varepsilon} &= 4\pi P \rho_1 \sigma^{-2} || \rho_0 \text{Re}\big(\boldsymbol{\Gamma}^H \boldsymbol{\varphi}\big) \odot \boldsymbol{f}_N + \rho_1 \boldsymbol{\Gamma}^H \boldsymbol{\Gamma} \boldsymbol{f}_N || \\
[\mathbb{I}]_{\rho_0,\rho_0} &= 2PNM\sigma^{-2} \\
[\mathbb{I}]_{\rho_0,\rho_1} &= 2P\sigma^{-2} || \text{Re}\big[\boldsymbol{\Gamma}^H \boldsymbol{\varphi}\big] || \\
[\mathbb{I}]_{\rho_0,\theta_{\text{Rx}}} &= 2P\rho_1\sigma^{-2} || \text{Re}\big[\frac{\partial \boldsymbol{\Gamma}^H}{\partial \theta_{\text{Rx}}} \boldsymbol{\varphi}\big] || \\
[\mathbb{I}]_{\rho_0,\varepsilon} &= 2P\rho_1\sigma^{-2} || \text{Im}\big[\boldsymbol{\Gamma} \boldsymbol{\varphi}^*\big] ||
\end{aligned}
$$

$$
\begin{aligned}
[\mathbb{I}]_{\rho_1,\rho_1} =& 2P\sigma^{-2}\mathrm{tr}\big(\mathbf{\Gamma}^H\mathbf{\Gamma}\big)\\
[\mathbb{I}]_{\rho_1,\theta_{\mathrm{Rx}}} =& 2P\rho_1\sigma^{-2}\mathrm{tr}\big(\mathrm{Re}\big[\frac{\partial\mathbf{\Gamma}^H}{\partial\theta_{\mathrm{Rx}}}\mathbf{\Gamma}\big]\big)\\
[\mathbb{I}]_{\rho_1,\varepsilon} =& 2P\rho_1\sigma^{-2}||\mathrm{Im}\big[\mathbf{\Gamma}^H\boldsymbol{\varphi}\big]||\\
[\mathbb{I}]_{\theta_{\mathrm{Rx}},\theta_{\mathrm{Rx}}} =& 2P\rho_1^2\sigma^{-2}\mathrm{tr}\big(\frac{\partial\mathbf{\Gamma}^H}{\partial\theta_{\mathrm{Rx}}}\frac{\partial\mathbf{\Gamma}}{\partial\theta_{\mathrm{Rx}}}\big)\\
[\mathbb{I}]_{\theta_{\mathrm{Rx}},\varepsilon} =& 2P\rho_1\sigma^{-2}||\mathrm{Im}\big[\frac{\partial\mathbf{\Gamma}^H}{\partial\theta_{\mathrm{Rx}}}\big(\rho_0\boldsymbol{\varphi}+\rho_1\mathrm{diag}(\mathbf{\Gamma})\big)\big]\big)\\
[\mathbb{I}]_{\varepsilon,\varepsilon} =& 2P\sigma^{-2}||\big[\rho_0^2+2\rho_0\rho_1\mathrm{Re}\big(\mathbf{\Gamma}\boldsymbol{\varphi}^*\big)+\rho_1^2\mathrm{diag}(\mathbf{\Gamma}^H\mathbf{\Gamma})\big]||
\end{aligned}
$$

B. Elements of the FIM for the two-BS-case

$$
\begin{aligned}
[\mathbb{I}_{\mathrm{BS}}]_{\tau_1,\tau_1} =& 8\pi^2P\rho_1^2\sigma^{-2}\boldsymbol{f}_N^T\boldsymbol{f}_N\\
[\mathbb{I}_{\mathrm{BS}}]_{\tau_1,\varepsilon_1} =& [\mathbb{I}_{\mathrm{BS}}]_{\varepsilon_1,\tau_1}=4\pi P\rho_1^2\sigma^{-2}||\boldsymbol{f}_N||\\
[\mathbb{I}_{\mathrm{BS}}]_{\tau_2,\tau_2} =& 8\pi^2P\rho_2^2\sigma^{-2}\boldsymbol{f}_N^T\boldsymbol{f}_N\\
[\mathbb{I}_{\mathrm{BS}}]_{\tau_2,\varepsilon_2} =& [\mathbb{I}_{\mathrm{BS}}]_{\varepsilon_2,\tau_2}=4\pi P\rho_2^2\sigma^{-2}||\boldsymbol{f}_N||\\
[\mathbb{I}_{\mathrm{BS}}]_{\rho_1,\rho_1} =& [\mathbb{I}_{\mathrm{BS}}]_{\rho_2,\rho_2}=2PMN\sigma^{-2}\\
[\mathbb{I}_{\mathrm{BS}}]_{\varepsilon_1,\varepsilon_1} =& 2P\rho_1^2MN\sigma^{-2}\\
[\mathbb{I}_{\mathrm{BS}}]_{\varepsilon_2,\varepsilon_2} =& 2P\rho_2^2MN\sigma^{-2}
\end{aligned}
$$

and the rest of the elements are equal to zero.